

Ab Initio Investigation of Electronic Properties using Density Functional Theory: MoSe₂ Monolayers

Amogh A*

© Copyrights Reserved

*Department of Physics, Birla Institute of Technology and Science, Pilani,
Hyderabad Campus, Jawahar Nagar, Hyderabad 500078, India.*

Abstract

Our work presents a detailed theoretical and first-principles study of the electronic properties of various monolayer MoSe₂ configurations, with a focus on their potential applications in electronic and optoelectronic devices. This study employs *ab initio* calculations based on density functional theory to calculate the materials' electronic band structure, density of states, and projected density of states. The band structure plot reveals the direct band gap of pristine MoSe₂ of about 1.43 eV at the K point, suggesting potential high-efficiency photodetectors and LEDs. The PDOS plots reveal the dominant contribution of Mo-*d* and Se-*p* orbitals in the valence and conduction bands. These findings establish monolayer MoSe₂ and its dopant variations as a reliable and versatile material with wide applications in electronic and optoelectronic systems.

1 Introduction

Molybdenum diselenide (MoSe₂), in recent years, has become the subject of many theoretical and experimental studies thanks to its unique combination of structural, electronic, and optical properties. MoSe₂ is a member of the transition metal dichalcogenides (TMDs), which are layered crystals with versatile properties. The monolayer MoSe₂ consists of a single layer of molybdenum atoms in between two layers of selenium atoms. The bulk structure of MoSe₂ shows an indirect band gap while the monolayer, remarkably, shows a direct band gap[33]. This makes it a great candidate in optical applications; direct band gap semiconductors are preferred to indirect ones because they eliminate the need for a phonon to assist in electronic transitions[33].

Each monolayer MoSe₂ comprises three atomic planes: a molybdenum plane sandwiched between two selenium planes. Molybdenum atoms are coordinated by selenium atoms in a trigonal prismatic geometry. MoSe₂ crystallises in a hexagonal phase

with space group P6₃/mmc[8]. In the bulk form, the layers of MoSe₂ are held together by weak van der Waals forces; thus, a monolayer can be obtained by the standard exfoliation technique[17]. This transition, because of the reduced dimensionality and quantum confinement, has profound effects on electronic properties. Specifically, the conduction band minima (CBM) shifts from the Γ point in the bulk to the K point in the monolayer, putting the band gap at a direct 1.43 eV instead of an indirect 1.1 eV[33].

The electronic properties of monolayer MoSe₂ are governed by its band structure, which gives the energy-momentum relationship of the electrons in the material. The CBM, located in the K-point of the Brillouin zone, is primarily composed of d_{z^2} orbitals, while the valence band minima (VBM) features contributions from selenium's *p* and molybdenum's *d* orbitals[13]. Spin-orbit coupling (SOC) introduces a band splitting of about 180 meV in the valence band. This could expand MoSe₂'s potential applications to spintronic devices as well[33]. The electronic density of states exhibits sharp peaks, called

*E-mail: f20220890@hyderabad.bits-pilani.ac.in

van Hove peaks[31], near the band edges corresponding to localised electronic states, critical for optical transitions and charge carrier dynamics.

Apart from the typical pristine MoSe₂ monolayers, we also explore the possible effects of oxygen doping and vacancy defects. Chalcogen defects are by far the most abundant point defects in 2D-TMDs[12]. Consequently, deviations in physical attributes, like electron transport characteristics, catalytic activity, and optical activity, from pristine MoSe₂ are attributed to these defects[18, 29, 30]. There is indirect evidence for this stemming from tunnelling electron microscopy (TEM) and scanning tunnelling electron microscopy (STM). It has to be noted, however, that introducing light substitutes like oxygen produces only a weak contrast in the TEM images, which could be misinterpreted as a chalcogen vacancy. In practice, chalcogen vacancies in TMDs can be introduced using chemical vapour deposition (CVD) or molecular beam epitaxy (MBE)[33]. The results can then later be verified using Raman spectroscopy or XRD[21]. Thus, the ability to manufacture a TMD-based electronic gadget depends on our ability to control the band gap as per the requirement.

2 Computational Details

We study the materials using density functional theory as implemented in Quantum ESPRESSO[26, 27, 25]. Our research involves a stepwise approach, consisting of parametric and structural optimisation, electronic structure analysis by studying the energy bands, the density of states (DOS), and projected (or partial) density of states (PDOS) simulations.

The first step is to optimise the computational parameters being used in all calculations. This is necessary as with the increase in cut-off energies and grid densities, numerical accuracy and, more importantly, computational time increase. A careful study of required accuracy and available computational resources has to be made, and the best cut-off has to be chosen. Convergence tests are carried out to ensure that the results are independent of the parameters and are accurate while being physically meaningful. The wave function and energy differences are confirmed to be well converged. This approach is necessary as it is comprehensive and robust against

variables and noise, and is accurate enough to draw important conclusions about the electronic properties of MoSe₂.

The next step is structure optimisation of MoSe₂, which is done to determine the equilibrium lattice parameters and atomic positions. This optimisation is performed using the Perdew–Burke–Ernzerhof (PBE) exchange-correlation functional within DFT[22]. The optimisation is done by adjusting the parameters a and c , and atomic positions until the Hellmann–Feynman forces on the atoms are minimised while ensuring energy convergence. This minimises the total energy of the system. A plane wave cut-off energy (`ecutwfc`) of 70 Ry is used while sampling the Brillouin zone with a **10×10×1** grid, ensuring quick and efficient convergence.

The actual calculations can now commence. The band structure of MoSe₂ is calculated to determine the electronic properties. This necessitates solving the Kohn-Sham equations at the high symmetry points (figure 8) to obtain the energy eigenvalues that dictate the energy dispersion. Numerically solve the Kohn-Sham eigenvalue equation

$$\hat{\mathcal{H}}_{KS} |\Psi_{n,\mathbf{k}}\rangle = E_{n,\mathbf{k}} |\Psi_{n,\mathbf{k}}\rangle, \quad (1)$$

where $\hat{\mathcal{H}}_{KS}$ is the Kohn-Sham Hamiltonian, $|\Psi_{n,\mathbf{k}}\rangle$ is the eigenfunction of the n^{th} state at a wave-vector \mathbf{k} , and $E_{n,\mathbf{k}}$ is the energy eigenfunction at the given point. This calculation provides insight into the electronic behaviour in the valence and conduction bands and the type of band gap: direct or indirect, a key characteristic useful for identifying optoelectronic applications.

The penultimate step is to find the electronic density of states (DOS), which tells the distribution of electronic states across different energy levels. The total DOS is computed by summing over all \mathbf{k} -points and energy bands:

$$g(E) = \sum_n \sum_{\mathbf{k}} \frac{\delta(E - E_{n,\mathbf{k}})}{N_{\mathbf{k}}}, \quad (2)$$

where $g(E)$ is the DOS at energy E , n is the band index, \mathbf{k} is the wave vector in the reciprocal space, $E_{n,\mathbf{k}}$ is the energy eigenvalue, and $N_{\mathbf{k}}$ is the number of points in Brillouin zone. The Dirac-Delta distribution is numerically approximated in many ways,

and here we present an efficient way to do so using a Gaussian:

$$\delta(E - E_{n,\mathbf{k}}) \approx \frac{1}{\sqrt{2\pi}\sigma} \exp\left(-\frac{(E - E_{n,\mathbf{k}})^2}{2\sigma^2}\right), \quad (3)$$

where σ controls the width of the “smearing” or spread. Only in the limit $\sigma \rightarrow 0$, the Gaussian will behave like a Dirac-Delta. Without smearing, the DOS plot would be a series of Dirac-Delta distributions, which is rather not helpful.

For the final step, we calculate the PDOS. This is to identify which electronic orbital contributes to the DOS at different energy ranges. PDOS, $g_\alpha(E)$, is given by:

$$g_\alpha(E) = \sum_n \sum_{\mathbf{k}} \frac{\delta(E - E_{n,\mathbf{k}})}{N_{\mathbf{k}}} \cdot \sum_r |\langle \alpha | \Psi_{n,\mathbf{k}} \rangle|^2, \quad (4)$$

where α indexes the orbital and $|\langle \alpha | \Psi_{n,\mathbf{k}} \rangle|^2$ captures the overlap of the total wave function $\psi_{n,\mathbf{k}}$ with orbital α .

3 Parameter Optimisation

3.1 Plane Wave Cutoff Energy

Plane waves of the form

$$\psi_{n,\mathbf{k}}(\mathbf{r}) = \sum_{\frac{|\mathbf{G}+\mathbf{k}|^2}{2} \leq E_{\text{cutwfc}}} C_{n,\mathbf{k}+\mathbf{G}} e^{i(\mathbf{k}+\mathbf{G}) \cdot \mathbf{r}} \quad (5)$$

are natural eigenfunctions of the translation operator, and since the lattice is periodic, potentials and charge densities can be represented in terms of this plane-wave set. The energies and forces in the system are calculated from the kinetic, potential, and exchange-correlation energies, which are all taken from the plane-wave calculations. We use the projector-augmented waves (PAW)[2, 14] method with the $4p$, $5s$, $4d$ valence states of the Mo atom, and the $4s$, $4p$ valence states of the Se atom.

Physically, `ecutwfc` corresponds to the maximum energy of the plane-wave being used in the Kohn-Sham wave function and only waves satisfying

$$\frac{1}{2}|\mathbf{k} + \mathbf{G}|^2 \leq \text{ecutwfc} \quad (6)$$

are kept. Quantum ESPRESSO implements this by making a 3D FFT grid whose density corresponds to

the specified cut-off.

`ecutrho` sets the maximum kinetic energy for expanding the electronic charge density $\rho(\mathbf{r})$. The charge density is calculated from the wave function as

$$\rho(\mathbf{r}) = \sum_n \sum_{\mathbf{k}} f_{n,\mathbf{k}} \langle \Psi_{n,\mathbf{k}} | \Psi_{n,\mathbf{k}} \rangle \quad (7)$$

where $f_{n,\mathbf{k}}$ denotes the occupation number with $0 \leq f_{n,\mathbf{k}} \leq 1$, and is given by the Fermi-Dirac distribution. In the case of a spin-polarised system, the summation runs separately over spin-up and spin-down states. While computing $\rho(\mathbf{r})$, \mathbf{G} -vectors of magnitude twice that of the basis can be generated. A sufficiently high value of `ecutrho` is necessary to accurately capture the high-frequency charge density oscillations which occur in areas of rapid spatial charge variation near ionic bonds or highly energetic systems.

Keeping a low `ecutrho` cut-off, less than 4-8 times `ecutwfc`, or even letting them be equal, aliases high-frequency components in $\rho(\mathbf{r})$ onto lower frequency ones, causing unphysical oscillations in total energy and forces. This is a well-documented phenomenon in Quantum ESPRESSO known as the “egg-box” effect, and some solutions have been proposed around it[6].

3.1.1 Time vs. Accuracy

Figure 1 shows the CPU time, in seconds, to run the `scf` calculation by varying only `ecutrho` and `ecutwfc`. It is noted that increasing either of those two increases computation time.

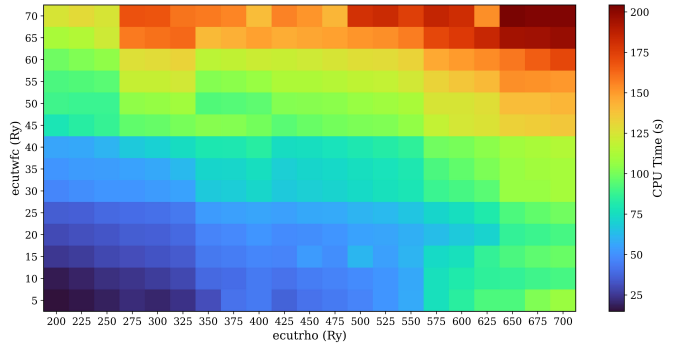


Figure 1: Heat map of CPU time (in seconds) plotted against `ecutrho` and `ecutwfc`

Figure 2 shows the accuracy of total energy obtained at the end of an `scf` calculation. The value obtained for `ecutwfc` = 70 and `ecutrho` = 700 was

taken as the reference, and the logarithm of the absolute difference with respect to the reference is plotted.

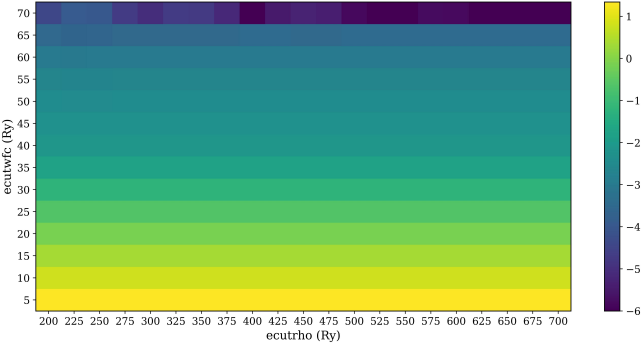


Figure 2: Heat map of total energy (in Ry) plotted against `ecutrho` and `ecutwfc`

3.1.2 Convergence vs. Cutoff

We plot, in figure 3, the total energy as a function of the two parameters, and it can be noted that the `scf` converges very quickly on increasing `ecutwfc` with little variation on increasing `ecutwfc` beyond 50 and `ecutrho` beyond 400. Thus, one could use `ecutrho = 400` and `ecutwfc = 50` for all calculations as it provides accurate results with less computational demands. It is also to be noted that these values should not go below what is recommended by the authors for the given pseudopotential. For our calculations, we used `ecutrho = 700` and `ecutwfc = 70`, ensuring maximum accuracy by spending a bit more computational resources.

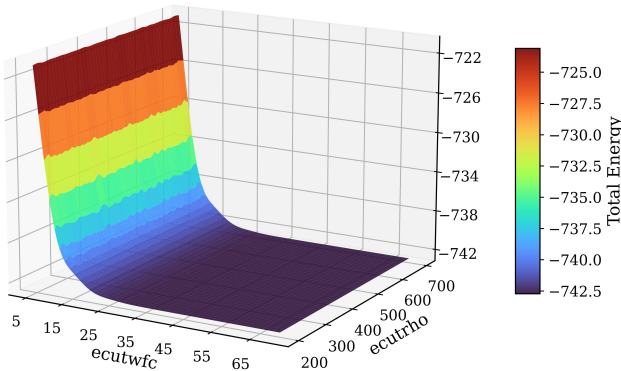


Figure 3: 3D surface plot of `ecutwfc`, `ecutrho`, and total energy (all in Ry)

Finally, we plot in figure 4, the CPU time versus `ecutwfc` for all values of `ecutrho` and fit it to a power law: $y = \alpha x^n$. We report $n = 1.32 \pm 0.21$, thus suggesting an $\mathcal{O}(n^{1.32})$ time complexity for the

parameter `ecutwfc`. The reported exponent is within 15% of the accepted time complexity for `ecutwfc` of $\mathcal{O}(n^{1.5})$ as reported in literature[5]. The error can be attributed to two factors: (1) $\mathcal{O}(n^{1.5})$ assumes an ideal plane-wave DFT, but our system has multiple atoms with inconsistent symmetry along different axes; (2) non-uniform computing environments stemming from environmental, thermal, and variable CPU loads.

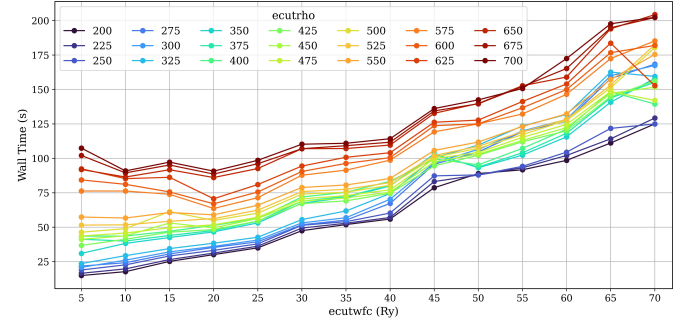


Figure 4: Power law fit of `ecutwfc` vs CPU Time for different `ecutrho`. $y = x^n; n = 1.32$

The exponent can be derived theoretically as the total number of electronic orbitals of energy $\epsilon \leq \epsilon_F$ is directly related to the maximum energy ϵ_F [11]. Let L be the periodicity of the lattice, ϵ_F be the maximum energy of a fermion, and k_ϵ be the wave vector for a given energy ϵ . Thus, in a sphere of volume $4\pi/3k_F^3$, you can have a maximum of

$$N(k_\epsilon) = 2 \left(\frac{4\pi k_\epsilon^3 / 3}{(2\pi/L)^3} \right) \quad (8)$$

fermionic states. The factor of two arises from the two allowed states of m_s , the spin quantum number of an electron. Knowing that $\epsilon = \hbar^2 k^2 / 2m$, N can be re-written as

$$N(\epsilon_F) = \frac{L^3}{3\pi^2} \left(\frac{2m\epsilon_F}{\hbar^2} \right)^{3/2}. \quad (9)$$

3.2 Lattice Parameters

The in-plane parameters a and b are equal, while the out-of-plane parameter c is distinct. We set $c = 20$ Å to eliminate any possible effects from periodic images along the z direction. We focused on optimising a , as this directly influences the materials' properties.

To determine the equilibrium lattice constant, a was systematically varied from 2.5 Å to 4.1 Å and the total energy was computed for each value. The equilibrium lattice constant thus corresponds to the value

at the minima of the energy. As seen in figure 5, the total energy first decreases with an increase in a , reaches a minimum at 3.20 \AA , and then increases with further expansion. This is consistent with experimental results which report the lattice constant for bulk MoSe₂ which have $a = 3.27\text{ \AA}$ [23].

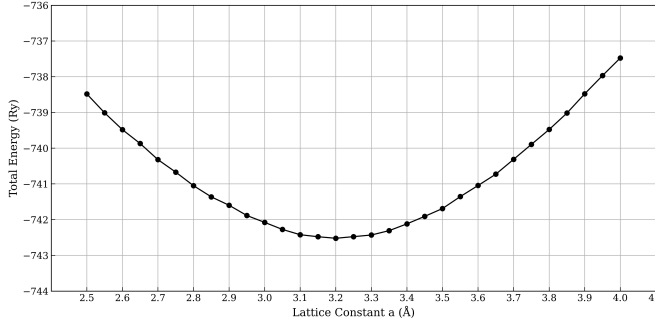


Figure 5: Total energy as a function of lattice parameter a .

3.3 Structural Relaxation

Following the optimisation of lattice parameters, the atomic coordinates of the structure were optimised so that they correspond to the true minimum of the system's total energy. While lattice parameter optimisation affects the overall cell dimensions, structural relaxation adjusts the atomic coordinates to minimise total energy and internal forces. This relaxation process was carried out iteratively in Quantum ESPRESSO using the conjugate gradient method, where in each step, the coordinates were adjusted based on the total energy and forces obtained in the previous step[24]. The iteration stops when the difference in energy and forces between successive iterations drops below a pre-set value. We set the process going until the forces converged within 10^{-5} Ry/Bohr and total energy within 10^{-4} Ry/Bohr . The maximum Hellmann-Feynman forces acting on each atom were less than 0.01 eV/\AA upon ionic relaxation. The pressure in the unit cell was kept below 5 kbar.

The final structure now corresponds to the true energy minima of the system, which is important as small deviations from the atomic positions can significantly affect the overall physical behaviour of the material.

3.4 K-point Sampling

The \mathbf{k} -point grid density is an important parameter in DFT calculations as it specifies the resolution of

the sampling in the reciprocal space. This is necessary as the accuracy of energy and electronic parameters depends on the accuracy of integration in the reciprocal space. Like most parameters mentioned till now, increasing \mathbf{k} -point density increases the accuracy of the calculations but also increases computational time. We

To optimise the \mathbf{k} -point grid, we varied the density from $1 \times 1 \times 1$ to $15 \times 15 \times 1$ (all grid densities in our calculations are fully Γ centred Monkhorst-Pack meshes[20]), ceteris paribus and plotted it against the total energy at the end of an **scf** calculation. Convergence was reached at $6 \times 6 \times 1$ with a variation of less than 0.001 Ry in further iterations.

We used a density of $10 \times 10 \times 1$ to capture the finer details at the high symmetry points and critical regions in the band structure. This ensures greater precision while being computationally feasible.

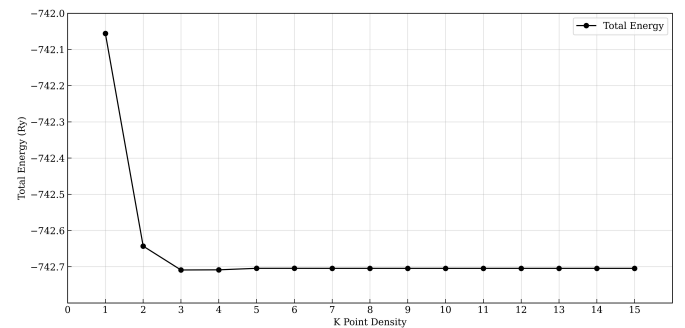


Figure 6: Convergence of total energy with increasing \mathbf{k} -grid density

4 Results and Discussion

4.1 Pristine MoSe₂

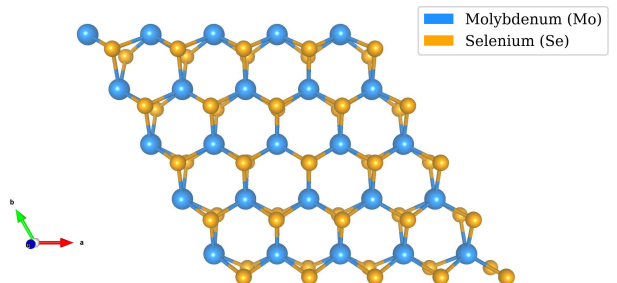


Figure 7: Pristine MoSe₂

4.1.1 Band structure

MoSe₂ settles in a hexagonal lattice with a lattice parameter of about 3.27 \AA [23]. The Wigner-Seitz cell

of this hexagonal lattice is another hexagon-shaped structure, as shown in figure 8.

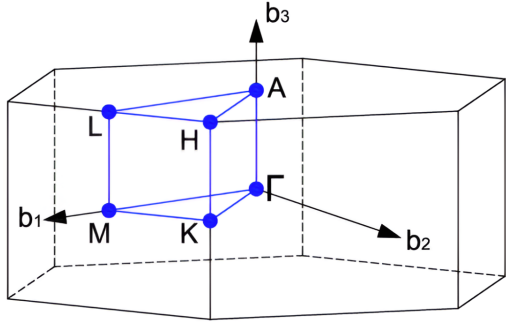


Figure 8: First Brillouin zone of a hexagonal lattice

We used a 75-step path to navigate between the high symmetry points in the sequence

$$\Gamma \rightarrow M \rightarrow K \rightarrow \Gamma \rightarrow A \rightarrow L \rightarrow H \rightarrow A$$

for all band structure calculations. Travelling from Γ to A should be a null relation as there are no states in the z direction and interactions with images along z are practically non-existent.

Our calculations show a direct band gap at the K point with a band gap of 1.43 eV, a figure slightly lower than the experimentally determined 1.5 eV[33]. This is a well-known problem with non-hybrid functionals like GGA, which underestimate the band gap as they do not accurately take the electron correlation into account[15]. The direct band gap corresponds to a photon of wavelength $\lambda = 867$ nm which is in the near-infrared (NIR) range. Thus, pristine MoSe₂ is a good candidate for high-efficiency optoelectronic devices like NIR-LEDs and NIR photodetectors[3].

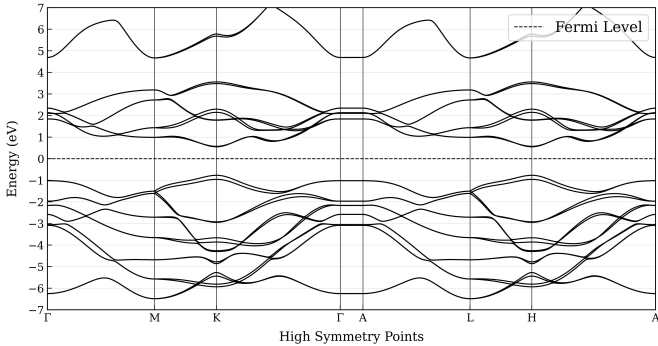


Figure 9: Band Structure of the pristine unit cell

4.1.2 Density of States

Near the Fermi level (set to 0 eV in all calculations), the DOS is shaped by the edges of the VB and CB.

The broad distribution of states in the VB reflects the hybridisation of Mo-*d* and Se-*p* orbitals. In the CB, the contribution is from Mo-*d* orbitals. The absence of states within the band gap confirms the semiconducting nature of MoSe₂. The van Hove peaks suggest a well-ordered crystalline periodicity, with strong electronic transitions at specific \mathbf{k} -points.

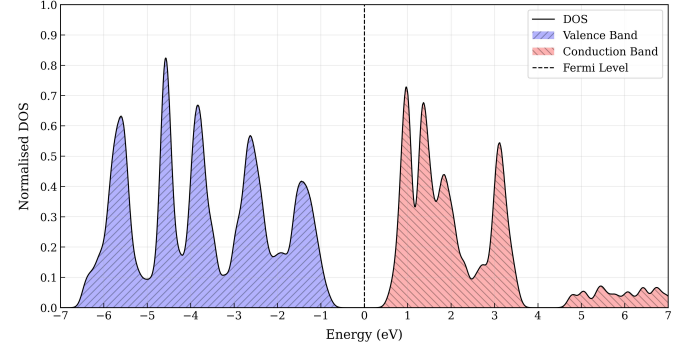


Figure 10: Density of States in pristine unit cell

4.1.3 Projected DOS

The conduction electrons in MoSe₂ are the Mo-*d* electrons, which dominate the electronic DOS above the Fermi level. They are instrumental in shaping the CBM at K point. The valence band is mostly composed of Mo-*p* and Se-*p* electrons with some contribution from Mo-*d* electrons. The VBM at K point also suggests strong hybridisation between Mo-*d* and Se-*p* electrons, indicative of the covalent interaction between Mo and Se. Strong hybridisation suggests robust electron-hole interactions, crucial for optoelectronic applications.

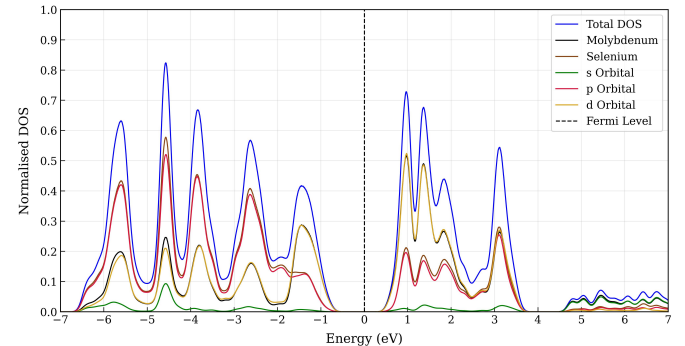


Figure 11: Projected DOS in pristine unit cell

4.1.4 Spin-Orbit Coupling

Another observation stems from the investigation of the effects of spin-orbit coupling (SOC) on the electronic band structure of MoSe₂. SOC is a relativistic effect where the intrinsic spin of the electron interacts

with the magnetic field generated by its orbital motion around the nucleus, which couples its spin with the orbital angular momentum. The Hamiltonian for SOC is given by

$$\mathcal{H}_{SO} = -\vec{\mu}_e \cdot \vec{B}, \quad (10)$$

where $\vec{\mu}_e = -g_0\mu_B\vec{s}$. The most famous example of SOC is the shifting of electronic energy levels observed as a splitting of spectral lines.

We carried out two calculations: one with SOC and one without. In the DFT + SOC calculations we use a non-collinear version of the PAW method and SOC is described using the spherical part of the Kohn-Sham potential inside the PAW spheres[9, 10].

In MoSe₂, the SOC effect comes about because of the heavy molybdenum atoms. A fully relativistic pseudopotential must be used to observe the effects of SOC in MoSe₂. As seen in figure 12, SOC introduces band splitting in the valence and conduction bands and is around 180 meV and 21 meV respectively. This is in spectacular agreement with the experimental results[23]. SOC also narrows the band gap from about 1.43 eV to 1.32 eV. These changes suggest a higher probability of an electronic transition from VB to CB; yet another indication of good optoelectronic behaviour. Note that there is no change in the nature of the band gap due to SOC; MoSe₂ is still a direct band gap semiconducting TMD at the K-point.

Another very important application of SOC is in valleytronics. Since MoSe₂ lacks inversion symmetry, and has direct band gaps at K and K' (K \pm), right (σ^+) and left (σ^-) circularly polarised light couple selectively; $\sigma^+ \rightarrow K+$ and $\sigma^- \rightarrow K-$ [32]. This has been experimentally observed through helicity-resolved photoluminescence in MoS₂[16, 28]. This opens up advanced optoelectronic applications, including valley-polarised luminescence, valley Hall currents, and optical control of exciton energies.

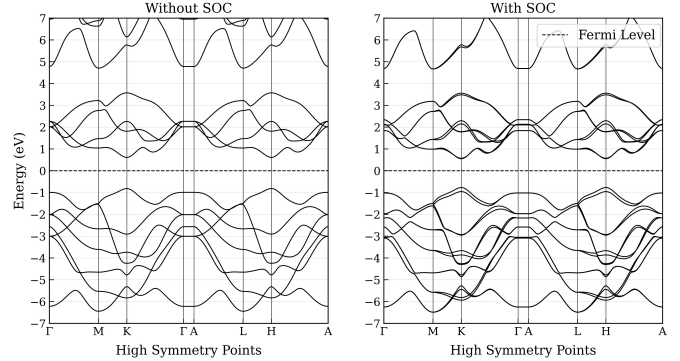


Figure 12: Effect of spin-orbit coupling on band structure in MoSe₂ unit cell

4.2 Oxygen Passivated MoSe₂

Since the OPM is a point defect in MoSe₂, there is no unit cell of size 1×1 as periodic repetitions of such a cell would not reproduce an OPM as seen in figure 13. We analysed the structure of a 5×5 supercell having a formula Mo₂₅Se₄₉O₁ with an oxygen concentration of 1.33%. Different supercells of suitable sizes must be constructed if analysis is needed at a particular doping concentration.

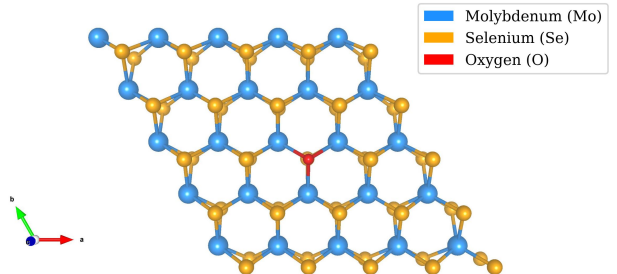


Figure 13: Oxygen Passivated MoSe₂

4.2.1 Band structure

In a crystal having lattice vector \mathbf{G} , states located at \mathbf{k} are equivalent to those at $\mathbf{k} + \mathbf{G}$. For a supercell, the physical volume is greater than its unit cell, and correspondingly, the Brillouin zone volume is smaller. Thus, traversing the full path $\Gamma \rightarrow M \rightarrow K \rightarrow \Gamma \rightarrow A \rightarrow L \rightarrow H \rightarrow A$ of the unit cell will map onto the super cell's Brillouin zone multiple times over. The lattice in the real space goes from periodicity a to na and the reciprocal space goes from $2\pi/a$ to $2\pi/na$, in the case of a 1D repetition. This is called band *folding*.

For the OPM, the band structure in figure 14 is the “unit cell” band structure, as a smaller cell with the same properties is not possible.

The VBM and CBM are clearly at the K point; thus, oxygen doping does not affect the underlying nature of the transitions. The band gap is reduced from 1.43 eV to around 1.27 eV. Oxygen acts as an electron acceptor, making OPM a p-type semiconductor.

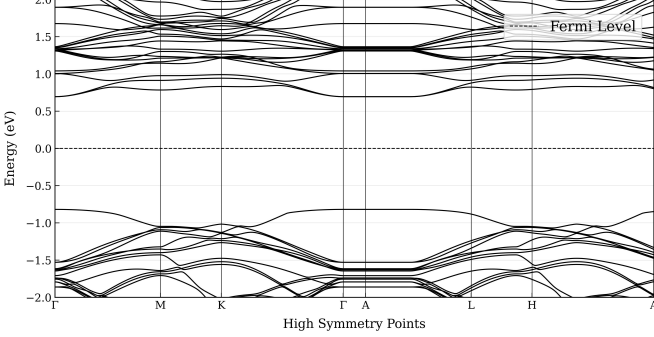


Figure 14: Band Structure in a 5×5 OPM

4.2.2 Density of States

Compared to pristine MoSe₂, OPM has larger and more pronounced electronic DOS in the conduction band. This suggests higher electron mobility and electrical conductivity. In this case, van Hove peaks are also seen, indicating the crystal's periodicity and symmetry are somewhat preserved. A slight shift in valence/conduction edges may reflect minor local lattice distortions or hybridisation due to the O atom. The oxygen atoms passivate any defect states and remove any non-radiative centres, boosting photoluminescence quantum yield (PLQY). OPM has a moderate-high electron mobility (compared to pristine) as it eliminates scattering centres, and tunes the band edge position, an instance of band gap engineering.

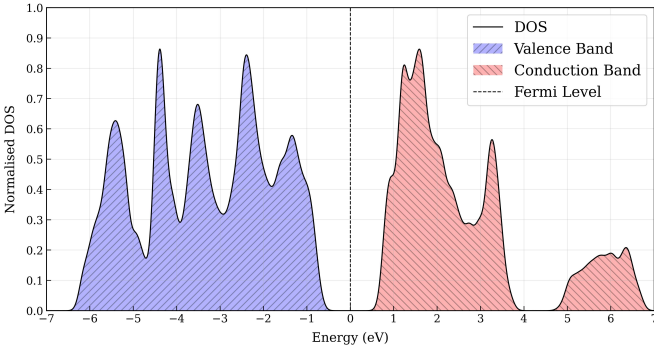


Figure 15: Density of States in a 5×5 OPM

4.2.3 Projected DOS

Similar to pristine MoSe₂, most of the valence band DOS comes from the hybridised Mo-*d* and Se-*p* or-

bitalis, and the conduction band DOS from Mo-*d* electrons. Owing to the low doping concentration, the electronic contribution from oxygen towards DOS is less. O substitution does not introduce mid-gap or near-Fermi states. It passivates the Se vacancy without disturbing the Mo-Se orbital hybridisation near the band edges. Thus, oxygen is a non-intrusive passivator.

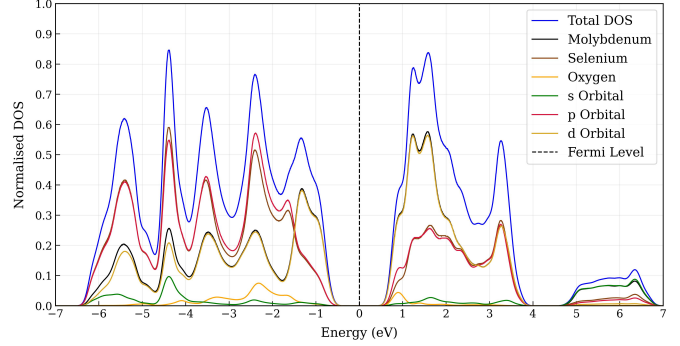


Figure 16: Projected DOS in a 5×5 OPM

4.3 Vacancy Defect MoSe₂

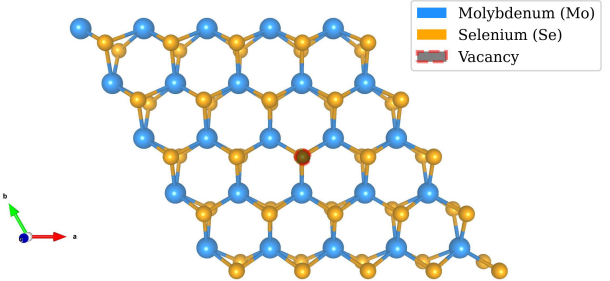


Figure 17: Vacancy Defect MoSe₂

Very similar to OPM, a 5×5 supercell had to be constructed and studied to understand the effects of chalcogen vacancies in TMDs. The vacancy concentration was 1.33% as 1 selenium atom was removed. Different-sized cells have to be constructed to understand the effects of vacancies of different concentrations and at different sites in the cell.

4.3.1 Band structure

New nearly flat bands appear $\approx 0.3 - 0.4$ eV above the valence-band maximum (blue line in figure 18). These are localised states arising from unsaturated Mo orbitals adjacent to the vacancy (see figure 17). Although the Fermi level still lies in the gap, the optical gap ($\text{VB} \rightarrow \text{defect state}$) is now smaller, around 1.1–1.3 eV. The Se vacancy acts as a shallow donor where free electrons can populate these levels and

become trapped, reducing PLQY via nonradiative recombination centres[18]. The flatness of the defect bands indicates very large effective masses; these centres will strongly scatter free carriers and degrade mobility by several orders of magnitude[4]. The defects also trap the charge carriers and reduce their lifetimes, significantly hurting the performance of a transistor made from this material, something which has been documented in MoS₂[7].

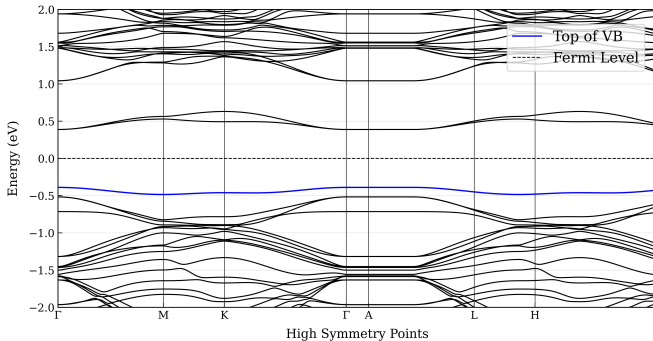


Figure 18: Band structure in a 5×5 VDM

4.3.2 Density of States

Finite DOS within the gap ($\approx 0.3 - 0.4$ eV above VB) confirms the presence of defect-induced mid-gap states. DOS almost goes to zero at the Fermi level, matching the near-flat defect bands seen in figure 18 (blue line). States in the gap allow sub-bandgap optical transitions (VB \rightarrow defect state), hurting the PLQY. The free electrons from VB can jump and get trapped in the donor level, which gives rise to Fermi level pinning, reducing the tunability of FETs, a phenomenon well documented for MoS₂[1].

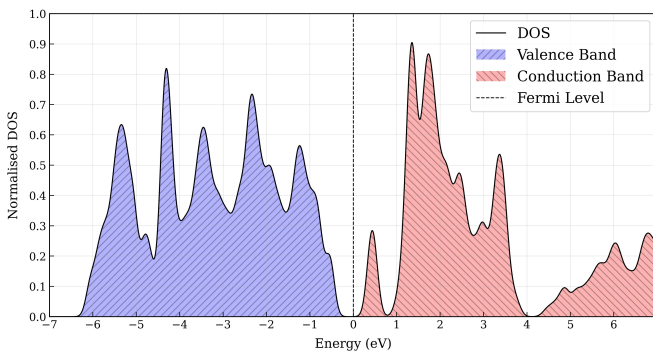


Figure 19: Density of States in a 5×5 VDM

4.3.3 Projected DOS

Se-*p* contribution near the Fermi level is reduced, reflecting the absence of one Se atom. Mid-gap states near the Fermi level are largely Mo-*d* derived, especially in the range -0.5 eV to 0.5 eV.

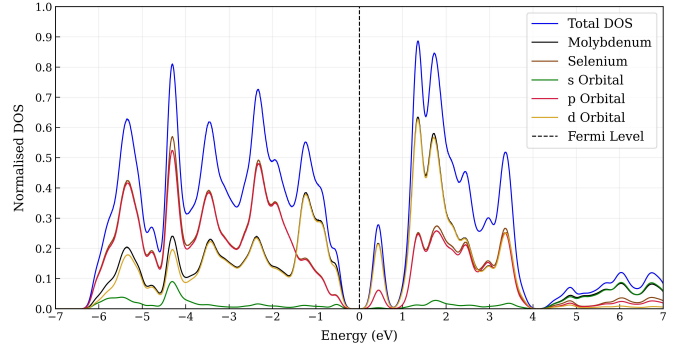


Figure 20: Projected DOS in a 5×5 VDM

5 Conclusions

From the discussions so far, it can be concluded that pristine MoSe₂ monolayers have high carrier mobility and PLQY. With a band gap of 1.43 eV, it is suited for NIR applications, and high mobility makes it a good choice for FETs. Oxygen passivated MoSe₂ has similar characteristics: moderate-high electron mobility with a 1.4 eV band gap, making it suited for defect-tolerant optoelectronics. Selenium vacancies in MoSe₂ are an issue as they introduce mid-gap states and pin the Fermi level, which are non-ideal when designing high-performance optoelectronics or FETs. It is also seen that the defect sites in MoSe₂ can be safely passivated by oxygen and can be used in devices which do not demand very high purity crystals.

6 Acknowledgements

We gratefully acknowledge the vast computing time provided on the High Performance Computing facility – Sharanga, at the Birla Institute of Technology and Science, Pilani, Hyderabad Campus.

We used pseudopotentials from the Quantum ESPRESSO pseudopotential database: <http://www.quantum-espresso.org/pseudopotentials>.

The structures presented in figure 7, figure 13, and figure 17 were visualised using VESTA[19].

7 Conflict of Interest

The author(s) declare that they have no known competing financial interests or personal relationships that could have appeared to influence the work reported in this paper.

8 Author Contributions

Amogh A: Conceptualization; Methodology; Data curation; Software; Formal analysis; Investigation; Visualization; Writing – original draft; Writing – review & editing.

9 References

- [1] Pantelis Bampoulis et al. “Defect Dominated Charge Transport and Fermi Level Pinning in *MoS₂*/Metal Contacts”. In: *ACS Applied Materials & Interfaces* 9.22 (2017). Published May 16, 2017, pp. 19278–19286. DOI: [10.1021/acsami.7b02739](https://doi.org/10.1021/acsami.7b02739). URL: <https://doi.org/10.1021/acsami.7b02739>.
- [2] P. E. Blöchl. “Projector Augmented-Wave Method”. In: *Physical Review B* 50 (1994), pp. 17953–17979. DOI: [10.1103/PhysRevB.50.17953](https://doi.org/10.1103/PhysRevB.50.17953).
- [3] Haitao Chen et al. “Manipulation of Photoluminescence of Two-Dimensional MoSe₂ by Gold Nanoantennas”. In: *Scientific Reports* 6 (2016), p. 22296. DOI: [10.1038/srep22296](https://doi.org/10.1038/srep22296). URL: <https://doi.org/10.1038/srep22296>.
- [4] Jiao Chen et al. “Tailoring Selenium Vacancies in MoSe₂ Through Oxygen Passivation for NO₂ Sensing Enhancement”. In: *Journal of Materials Chemistry A* 11.13 (2023), pp. 6171–6179. DOI: [10.1039/D3TA00376H](https://doi.org/10.1039/D3TA00376H). URL: <https://doi.org/10.1039/D3TA00376H>.
- [5] Kamal Choudhary and Francesca Tavazza. “Convergence and Machine Learning Predictions of Monkhorst-Pack k-points and Plane-Wave Cut-Off in High-Throughput DFT Calculations”. In: *arXiv preprint* (2018). Analyzes scaling behavior and cutoff convergence across 30k+ materials. URL: <https://arxiv.org/abs/1809.01753>.
- [6] B. Durham, M. I. J. Probert, and P. J. Hasnip. “Beating the Egg-Box Effect in Plane-Wave DFT Simulations”. In: *Electronic Structure* 7.2 (2025), p. 025004. DOI: [10.1088/2516-1075/adc056](https://doi.org/10.1088/2516-1075/adc056).
- [7] “Electron Transport Through the Multiple Sulfur Vacancies in MoS₂”. In: *Current Applied Physics* 57 (2024), pp. 20–25. ISSN: 1567-1739. DOI: <https://doi.org/10.1016/j.cap.2023.10.008>.
- [8] Eve D. Hanson et al. “Phase Engineering and Optical Properties of 2D MoSe₂: Promise and Pitfalls”. In: *Materials Chemistry and Physics* 225 (2019), pp. 219–226. DOI: [10.1016/j.matchemphys.2018.11.069](https://doi.org/10.1016/j.matchemphys.2018.11.069). URL: <https://www.sciencedirect.com/science/article/pii/S0254058418310277>.
- [9] D. Hobbs, G. Kresse, and J. Hafner. “Fully Unconstrained Noncollinear Magnetism Within the Projector Augmented-Wave Method”. In: *Physical Review B* 62 (2000), pp. 11556–11570. DOI: [10.1103/PhysRevB.62.11556](https://doi.org/10.1103/PhysRevB.62.11556).
- [10] Y.-S. Kim, K. Hummer, and G. Kresse. “Accurate Band Structures and Effective Masses for InP, InAs, and InSb using Hybrid Functionals”. In: *Physical Review B* 80 (2009), p. 035203. DOI: [10.1103/PhysRevB.80.035203](https://doi.org/10.1103/PhysRevB.80.035203).
- [11] Charles Kittel. *Introduction to Solid State Physics*. 8th. Hoboken, NJ: John Wiley & Sons, 2005. ISBN: 978-0-471-41526-8.
- [12] Kyungmin Ko et al. “Native Point Defects in 2D Transition Metal Dichalcogenides: A Perspective Bridging Intrinsic Physical Properties and Device Applications”. In: *Journal of Applied Physics* 135.10 (2024), p. 100901. DOI: [10.1063/5.0185604](https://doi.org/10.1063/5.0185604).
- [13] K. Kośmider, J. W. González, and J. Fernández-Rossier. “Large Spin Splitting in the Conduction Band of Transition Metal Dichalcogenide Monolayers”. In: *Physical Review B* 88 (2013), p. 245436. DOI: [10.1103/PhysRevB.88.245436](https://doi.org/10.1103/PhysRevB.88.245436).
- [14] G. Kresse and D. Joubert. “From Ultrasoft Pseudopotentials to the Projector Augmented-Wave Method”. In: *Physical Review B* 59 (1999), pp. 1758–1775. DOI: [10.1103/PhysRevB.59.1758](https://doi.org/10.1103/PhysRevB.59.1758).
- [15] Timo Lebeda et al. “Right band gaps for the right reason at low computational cost with a meta-GGA”. In: *Physical Review Materi-*

- als 7.9 (2023), p. 093803. DOI: [10.1103/PhysRevMaterials.7.093803](https://doi.org/10.1103/PhysRevMaterials.7.093803).
- [16] Kin Fai Mak et al. “Control of Valley Polarization in Monolayer MoS₂ by Optical Helicity”. In: *Nature Nanotechnology* 7 (2012), pp. 494–498. DOI: [10.1038/nano.2012.96](https://doi.org/10.1038/nano.2012.96). URL: <https://doi.org/10.1038/nano.2012.96>.
- [17] E. Pollmann et al. “How High is a MoSe₂ Monolayer?” In: *Nanotechnology* (2022). arXiv:2109.05354.
- [18] Yuze Meng et al. “Repairing Atomic Vacancies in Single-Layer MoSe₂ Field-Effect Transistor and its Defect Dynamics”. In: *arXiv preprint arXiv:1601.05534* (2016). Combined TEM, Raman and DFT insights on vacancy repair and mobility improvement. DOI: [10.1103/1.4999524](https://doi.org/10.1103/1.4999524).
- [19] Koichi Momma and Fujio Izumi. “VESTA: A Three-Dimensional Visualization System for Electronic and Structural Analysis”. In: *Journal of Applied Crystallography* 41 (2008), pp. 653–658. DOI: [10.1107/S0021889808012016](https://doi.org/10.1107/S0021889808012016). URL: <https://doi.org/10.1107/S0021889808012016>.
- [20] H. J. Monkhorst and J. D. Pack. “Special Points for Brillouin-zone Integrations”. In: *Physical Review B* 13 (1976), pp. 5188–5192. DOI: [10.1103/PhysRevB.13.5188](https://doi.org/10.1103/PhysRevB.13.5188).
- [21] Zhiwei Peng et al. “Strain Engineering of 2D Semiconductors and Graphene: From Strain Fields to Band-Structure Tuning and Photonic Applications”. In: *Light: Science and Applications* 9.1 (2020), p. 190. DOI: [10.1038/s41377-020-00421-5](https://doi.org/10.1038/s41377-020-00421-5). URL: <https://doi.org/10.1038/s41377-020-00421-5>.
- [22] J. P. Perdew, K. Burke, and M. Ernzerhof. “Generalized Gradient Approximation Made Simple”. In: *Physical Review Letters* 77 (1996), pp. 3865–3868. DOI: [10.1103/PhysRevLett.77.3865](https://doi.org/10.1103/PhysRevLett.77.3865).
- [23] J. Picker, M. Schaal, and A. Turchanin. “Structural and Electronic Properties of MoS₂ and MoSe₂ Monolayers Grown by Chemical Vapor Deposition on Au(111)”. In: *Nanoscale Advances* (2023). URL: <https://www.ncbi.nlm.nih.gov/pmc/articles/PMC10729873/>.
- [24] Quantum ESPRESSO Developers. *Quantum ESPRESSO: CP (Car-Parrinello) User Guide*. Accessed: 2025-06-10. Quantum ESPRESSO Foundation. 2023. URL: https://www.quantum-espresso.org/Doc/user_guide_PDF/cp_user_guide.pdf.
- [25] P. Giannozzi et al. “Quantum ESPRESSO: A Modular and Open-Source Software Project for Quantum Simulations of Materials”. In: *Journal of Physics: Condensed Matter* 21.39 (2009), p. 395502. URL: <http://www.quantum-espresso.org>.
- [26] P. Giannozzi et al. “Advanced Capabilities for Materials Modelling with Quantum ESPRESSO”. In: *Journal of Physics: Condensed Matter* 29.46 (2017), p. 465901. URL: <http://stacks.iop.org/0953-8984/29/i=46/a=465901>.
- [27] P. Giannozzi et al. “Quantum ESPRESSO Toward the Exascale”. In: *The Journal of Chemical Physics* 152.15 (2020), p. 154105. DOI: [10.1063/5.0005082](https://doi.org/10.1063/5.0005082).
- [28] John R. Schaibley et al. “Valleytronics in 2D Materials”. In: *Nature Reviews Materials* 1 (2016), p. 16055. DOI: [10.1038/natrevmats.2016.55](https://doi.org/10.1038/natrevmats.2016.55). URL: <https://doi.org/10.1038/natrevmats.2016.55>.
- [29] Alina Shafqat, Tahir Iqbal, and Abdul Majid. “A DFT Study of Intrinsic Point Defects in Monolayer MoSe₂”. In: *AIP Advances* 7.10 (2017), p. 105306. DOI: [10.1063/1.4999524](https://doi.org/10.1063/1.4999524).
- [30] Haibo Shu et al. “Defect Engineering in MoSe₂ for the Hydrogen Evolution Reaction”. In: *ACS Applied Materials and Interfaces* 9.50 (2017), pp. 43648–43656. DOI: [10.1021/acsami.7b12478](https://doi.org/10.1021/acsami.7b12478).
- [31] Léon van Hove. “The Occurrence of Singularities in the Elastic Frequency Distribution of a Crystal”. In: *Physical Review* 89.6 (Mar. 1953), pp. 1189–1193. DOI: [10.1103/PhysRev.89.1189](https://doi.org/10.1103/PhysRev.89.1189).
- [32] Jun Xiao et al. “The Interaction of 2D Materials With Circularly Polarized Light”. In: *Advanced Science* 10.9 (2023), p. 2206191. DOI: [10.1002/advs.202206191](https://doi.org/10.1002/advs.202206191). URL: <https://doi.org/10.1002/advs.202206191>.

- [33] Yi Zhang et al. “Direct Observation of the Transition from Indirect to Direct Bandgap in Atomically Thin Epitaxial MoSe₂”. In: *Nature Nanotechnology* 9.2 (2013), pp. 111–115. DOI: 10.1038/nnano.2013.277. URL: <http://dx.doi.org/10.1038/nnano.2013.277>.